J. Fluid Mech. (2005), *vol.* 528, *pp.* 119–133.
doi:10.1017/S0022112004003180 Printed in the United Kingdom

Multicellular convection in rotating annuli

By E. PLAUT[1] AND F. H. BUSSE[2]

[1]LEMTA, INPL – UHP – CNRS, 2 av. de la Forêt de Haye, F-54516 Vandoeuvre cedex, France

[2]Institute of Physics, University of Bayreuth, D-95440 Bayreuth, Germany

(Received 5 April 2004 and in revised form 28 October 2004)

The onset of convection in a rotating cylindrical annulus with sloping conical boundaries is studied in the case where this slope increases with the radius. The critical modes assume the form of drifting spiralling columns attached to the inner cylindrical wall at moderate and large Prandtl numbers, but they become attached to the outer wall at low Prandtl numbers. These latter 'equatorially attached' modes are multicellular at intermediate rotation rates. Through a perturbation analysis which is validated by a numerical code, we show that all equatorially attached modes are quasi-inertial modes and analyse the physical mechanisms leading to multicells. This is done for both stress-free and no-slip boundary conditions. At finite amplitudes the convection generates a Reynolds stress which leads to the development of a mean zonal flow, and a geometrical analysis of the mechanisms leading to this zonal flow is presented. The influence of Ekman friction on the zonal flow is also studied.

1. Introduction

The problem of the convection driven by centrifugal buoyancy in rotating cylindrical annuli has received considerable attention in recent years (see, e.g. Abdulrahman *et al.* 2000; Pino *et al.* 2000, 2001; Plaut & Busse 2002; Westerburg & Busse 2003; Aubert, Gillet & Cardin 2003; Morin & Dormy 2004) because it serves as a model for the more complex dynamics of convection in rotating spherical fluid shells. This latter problem is one of the fundamental problems in geophysics and astrophysics in that it provides the basis for the understanding of the energy transport from the interior of celestial bodies and of the generation of magnetic fields by the associated fluid flows. While the problem of convection in rotating spheres depends on three spatial coordinates as well as on time, the dependence on the third coordinate in the direction of the axis of rotation can be eliminated in the analysis of the corresponding rotating cylindrical annulus problem. For introductions to this 'quasigeostrophic' approach we refer to the original publication Busse (1970) as well as Busse & Or (1986).

In the case of convection in a rotating spherical fluid shell Zhang & Busse (1987) and Zhang (1992) have shown that there actually exist two different types of critical mode. Thermal Rossby waves in the form of drifting spiralling columns describe the onset of convection for moderate and large values of the Prandtl number P. The extent of spiralling increases with decreasing P, while at high values of P the columns are more confined and the spiralling is less noticeable; the complete asymptotic theory for these spiralling modes has been obtained only recently by Dormy *et al.* (2004). At low values of the Prandtl number P, convection cells attached to the outer equator of the shell are preferred. These 'equatorially attached modes' can be interpreted as modified inertial waves and, indeed, Zhang (1993, 1994) was able to determine

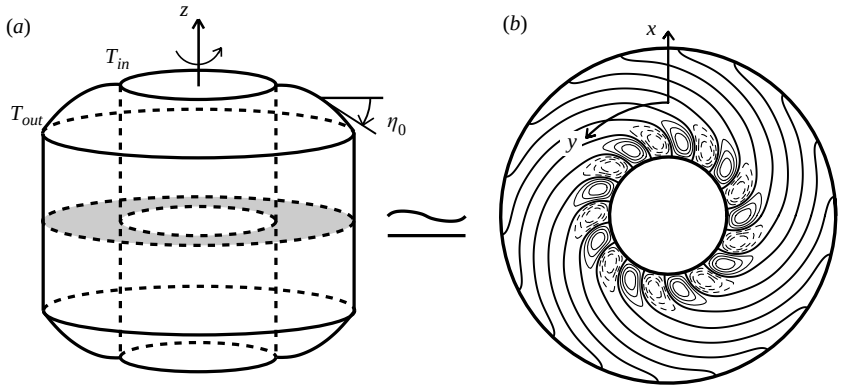

FIGURE 1. (*a*) Geometry of the rotating cylindrical annulus. The fluid is contained in a cylindrical channel spinning around its z-axis. A radial temperature difference $T_{out} - T_{in}$ is imposed at the vertical sidewalls. The conical caps are curved. After integration over the axial coordinate z, we are led to a two-dimensional problem in the equatorial (grey) plane. (*b*) Streamlines of a spiralling neutral mode computed with the Galerkin code for stress-free boundary conditions, $\epsilon = 2$, $P = 1$, $\eta = 42\,000$. The annular geometry has been reconstructed from the Cartesian solution $\psi(x, y, t)$ by applying the transformation $(x, y) \mapsto (r_m + x)(\cos(y/r_m), \sin(y/r_m))$ with the dimensionless mid-radius $r_m = 1.04$ (see § 3).

their properties through a perturbation analysis based on inertial oscillations as solutions of lowest order. For an extension of this approach, see Busse & Simitev (2004).

A salient feature of the critical equatorially attached modes, discovered by Yano (1992) in the framework of a quasi-geostrophic model, and confirmed by the numerical study of Ardes, Busse & Wicht (1997) for three-dimensional spherical shell convection, is that they are multicellular at large rotation rates. Similar multicellular modes have also been found by Pino *et al.* (2000) in the analysis of the onset of convection in a rotating annulus with a finite gap between the cylindrical boundaries. Yano (1992) suggested that all convection modes of a cylindrical annulus attached to the outer wall, including the multicellular ones, are modified inertial waves. However, his treatment is not entirely satisfactory because only quite large rotation rates were considered, in terms of the Ekman number E, $E^{-1} \gg P^{-5/2}$ where P is small (see his equation 2.7*e* and the first inequality in his Appendix C). Moreover, it was assumed that the radial length-scale of the convection modes is much smaller than the gap width. As a result only the boundary condition at the outer wall has been taken into account.

The goal of this paper is to present an analysis of the multicellular convection in a simple framework. For this purpose we use the small-gap approximation, but include the effect of curved conical boundaries which is necessary for the spiralling (figure 1) as well as the equatorially attached (figure 2) modes. For the description of the latter we develop an asymptotic theory which establishes that they are all modified inertial waves, and which is valid for $E^{-1} \gtrsim P^{-1}$ and small P. In a second part of the paper, we study some relevant nonlinear effects proportional to the square of the convection amplitude, namely the generation of mean flows or 'zonal flows'.

An outline of the paper is as follows. In § 2 the mathematical formulation of the model is given at linear order in the convection amplitudes. In § 3 the results of a numerical stability analysis are presented. Section 4 is devoted to the description of the inertial modes with stress-free boundaries. In § 5 the corresponding marginal stability

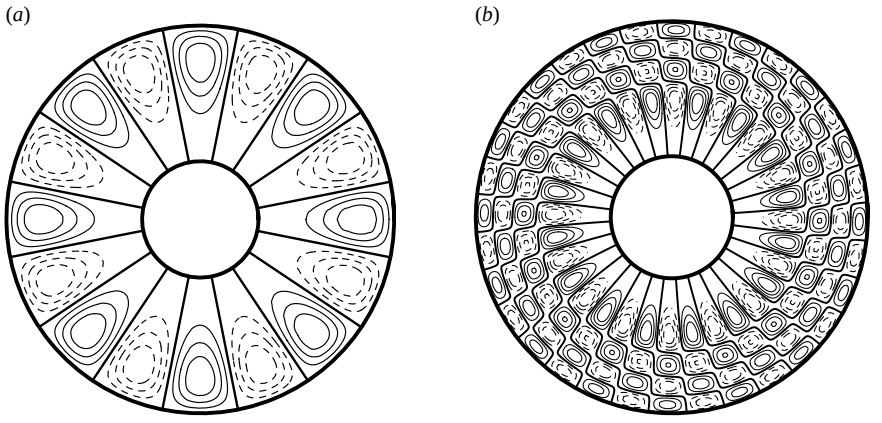

FIGURE 2. Streamlines computed with the Galerkin code for stress-free boundary conditions and shown with an annular display as in figure 1(*b*): (*a*) an equatorially attached neutral mode at $\epsilon = 2$, $P = 10^{-4}$, $\eta = 6 \times 10^5$, $r_m = 0.93$; (*b*) a multicellular equatorially attached critical mode at $\epsilon = 2$, $P = 0.025$, $\eta = 8 \times 10^5$, $r_m = 0.95$.

curves for the convection problem are obtained in the limit of very low Prandtl numbers. The case of no-slip boundaries is studied in § 6. Section 7 is devoted to the study of the generation of mean flows. A more general discussion, which includes in particular a consideration of the Ekman friction effects neglected up to § 7, is given in § 8, before the conclusion.

2. Mathematical model for linear waves

A cylindrical annulus rotating rigidly about its axis of symmetry with the angular velocity Ω, as shown in figure 1, is considered. The inner cylindrical wall is kept at temperature T_{in}, while the temperature of the outer wall is fixed at the higher value T_{out}. Using the gap width d as the length scale, d^2/ν as the time scale, where ν is the kinematic viscosity of the fluid, and $P(T_{out} - T_{in})$ as the scale of the temperature, we write the equations of motion for the velocity field $\boldsymbol{v}$ and the heat equation for the deviation θ of the temperature from the basic profile of pure conduction in dimensionless form

$$\partial_t \boldsymbol{v} + (\boldsymbol{v} \cdot \nabla)\boldsymbol{v} + 2E^{-1}\hat{\boldsymbol{z}} \times \boldsymbol{v} = -\nabla p - R\theta\hat{\boldsymbol{x}} + \Delta \boldsymbol{v}, \tag{2.1a}$$

$$\nabla \cdot \boldsymbol{v} = 0, \tag{2.1b}$$

$$P(\partial_t \theta + \boldsymbol{v} \cdot \nabla\theta) = -v_x + \Delta\theta. \tag{2.1c}$$

In (2.1), the Ekman, Rayleigh and Prandtl numbers are

$$E = \nu/(d^2\Omega), \quad R = \gamma g d^3 (T_{out} - T_{in})/(\kappa\nu), \quad P = \nu/\kappa,$$

where γ and κ are the coefficient of thermal expansion and the thermal diffusivity of the fluid, respectively, and g is the average centrifugal acceleration. We have assumed the small-gap approximation which allows the use of the Cartesian coordinates x, y and z as shown in figure 1. The boundary conditions are given by

$$v_x = \partial_x^2 v_x = \theta = 0 \quad \text{at} \quad x = \pm 1/2, \tag{2.2}$$

$$v_z = \mp\eta_0(1 + \epsilon x)v_x \quad \text{at} \quad z = \pm h/2d, \tag{2.3}$$

where the cylindrical walls of average height h are assumed to be stress-free and $\eta_0(1+\epsilon x)$ denotes the small angle between the conical end surfaces and the equatorial plane. For $\epsilon = 0$, this angle is constant while a finite curvature of the cones is described by finite values of ϵ. The case of no-slip cylindrical walls may also be considered, in which case condition (2.2) must be replaced by

$$v_x = \partial_x v_x = \theta = 0 \quad \text{at } x = \pm\tfrac{1}{2}. \tag{2.4}$$

Since η_0 is a small parameter, the solution of (2.1) can be described in first approximation by its geostrophic part

$$\boldsymbol{v} = \nabla\psi(x, y, t) \times \hat{\mathbf{z}} + O(\eta_0), \quad \theta = \theta(x, y, t) + O(\eta_0). \tag{2.5}$$

By taking the z-component of the curl of (2.1a), averaging it over the height of the annulus and using conditions (2.3) we obtain, for linear waves of small amplitude,

$$-\partial_t \Delta_2 \psi + \eta(1+\epsilon x)(\partial_y \psi) = -\Delta_2 \Delta_2 \psi + R\partial_y \theta, \tag{2.6}$$

where $\Delta_2 = \partial_x^2 + \partial_y^2$ is the two-dimensional Laplacian and the Coriolis parameter η is defined by

$$\eta = 4E^{-1}(d/h)\eta_0.$$

For a more detailed discussion, see, for example, Busse & Or (1986). Neutral wave solutions of (2.6) and (2.1c), of the form

$$\psi(x, y, t) = 2\mathrm{Re}\{\Psi(x)\exp[\mathrm{i}(\alpha y - \omega t)]\}, \tag{2.7a}$$

$$\theta(x, y, t) = 2\mathrm{Re}\{\Theta(x)\exp[\mathrm{i}(\alpha y - \omega t)]\}, \tag{2.7b}$$

must therefore satisfy

$$\left[\mathrm{i}\omega\left(\partial_x^2 - \alpha^2\right) + \mathrm{i}\alpha\eta(1+\epsilon x)\right]\Psi(x) = -\left(\partial_x^2 - \alpha^2\right)^2\Psi(x) + \mathrm{i}\alpha R\Theta(x), \tag{2.8a}$$

$$-\mathrm{i}\omega P\Theta(x) = \left(\partial_x^2 - \alpha^2\right)\Theta(x) - \mathrm{i}\alpha\Psi(x), \tag{2.8b}$$

the boundary conditions being either

$$\Psi = \partial_x^2\Psi = \Theta = 0 \quad \text{at } x = \pm\tfrac{1}{2} \text{ in the stress-free case,} \tag{2.9a}$$

or

$$\Psi = \partial_x\Psi = \Theta = 0 \quad \text{at } x = \pm\tfrac{1}{2} \text{ in the no-slip case,} \tag{2.9b}$$

according to (2.2) and (2.4).

In order to assess the validity of the asymptotic theories that will be developed, and to be able also to address the case of large Prandtl numbers, we use a Galerkin method to solve numerically the linear problem (2.8), (2.9).

3. Results of the linear Galerkin code: nature of the critical modes

The linear Galerkin code shows that spiralling modes attached to the inner boundaries are preferred at large P and large η. An example of such a spiralling critical mode, computed with stress-free boundary conditions, is displayed in figure 1(b) through the isolines of the real streamfunction, (2.7a). For all our streamline patterns, the streamfunction levels are evenly spaced, thick lines showing the separatrices $\psi = 0$, full lines the positive levels of ψ, dashed lines the negative levels of ψ. Despite the fact that the small-gap approximation is questionable, the similarity of the pattern in figure 1(b) with those obtained by Aubert *et al.* (2003) in their figure 3 from two- and three-dimensional computations is remarkable. Note that in figure 1(b) only the

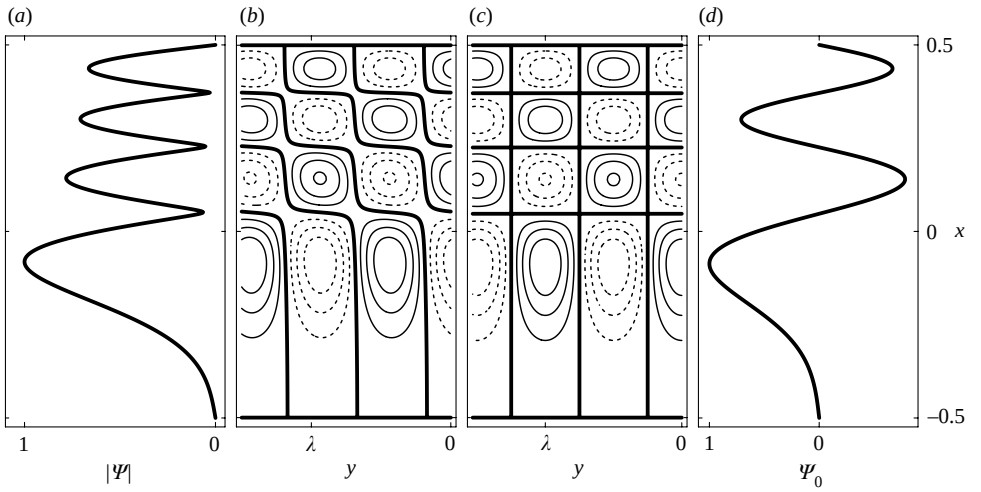

FIGURE 3. (*a*) Modulus of the streamfunction $\Psi(x)$ and (*b*) streamlines of the multicellular equatorially attached critical mode of figure 2(*b*), now with the natural Cartesian display of our model. The wavelength $\lambda = 2\pi/\alpha_c = 0.374$. (*c*) Streamlines and (*d*) streamfunction $\Psi_0(x)$ of the critical inertial mode computed for the same parameters (see §§4 and 5 and the data at $\eta P = 20\,000$, figure 8).

separatrices cover the whole gap, since the modulus of the streamfunction decreases rapidly with increasing x. An example of spiralling mode computed with no-slip boundary conditions is displayed in figure 10(*a*); the decrease of the streamfunction with increasing x is made clear with the dotted curve in figure 10(*b*). Note that the balances involved in the selection of spiralling modes are subtle, since, even for quite large P, there remain three important terms in equation (2.8*a*), namely the Coriolis, viscous and buoyancy terms. Moreover, the streamfunction Ψ cannot be rescaled to be real, and the problem to be solved, even in the asymptotic limit of very large rotation rates, is essentially complex (see e.g. Jones, Soward & Mussa 2000).

For small P, equatorially attached modes are obtained, which present large moduli of the streamfunction near the outer cylinder. Such modes are displayed in figure 2. Despite the small-gap approximation and the fact that in a spherical shell the slope of the end surfaces is quite large in the region near the outer equator, the monocellular mode in figure 2(*a*) is still rather close to those obtained from three-dimensional computations in a spherical shell in figure 12 of Simitev & Busse (2004). The fact that the separatrices are straight lines in figure 2(*a*) indicates that the streamfunction Ψ can be rescaled to be real. For faster rotation rates, i.e. larger values of η, multicellular equatorially attached modes are preferred, as that shown in figures 2(*b*) and 3(*a*, *b*) for stress-free boundary conditions; for no-slip boundary conditions, see figure 11(*a*). The modulus of the complex streamfunction shows four local maxima in figure 3(*a*), hence, we denote this mode as an $n = 4$ equatorially attached mode. It is worth noting here also the similarity of the patterns in figures 2(*b*) and 3(*b*) with three-dimensional results for spherical shell convection, namely those of figure 6 of Ardes *et al.* (1997).

Considering naturally, in the framework of our small-gap approximation, the wavenumber α as a continuous parameter, we have performed a systematic computation of the critical mode, i.e. the neutral mode with the lowest value of R. This leads, for stress-free boundary conditions and $\epsilon = 2$, to the diagram in figure 4. For $P \gtrsim 0.15$, the transition between equatorially attached modes at small η and spiralling modes

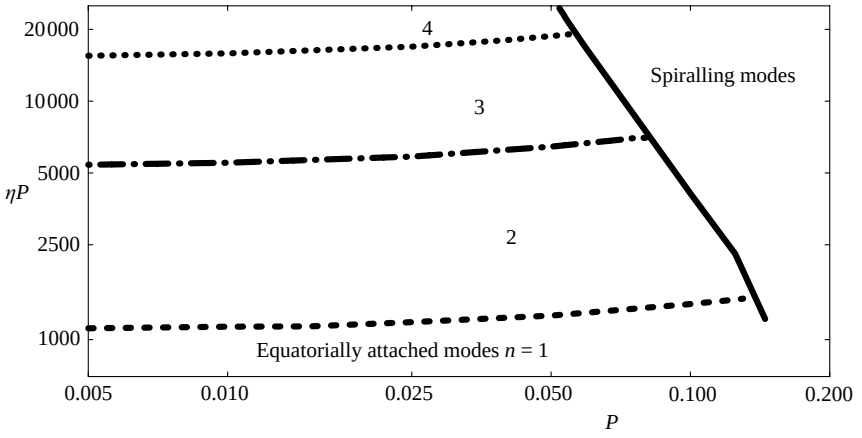

FIGURE 4. Nature of the critical modes computed with the Galerkin code for stress-free boundary conditions and $\epsilon = 2$.

at large η is not sharp, therefore we have not drawn any transition line in this region. For smaller values of the curvature parameter ϵ, the diagram looks similar, at least in the lower left-hand region; however, all transition lines are shifted to larger values of η. Moreover, for $\epsilon \lesssim 0.5$, at fixed P the transition towards spiralling modes at large η is smooth, and the extrema of $|\Psi(x)|$ are much less pronounced than in the case of figure 3(a); the number n of maxima increases and then decreases with increasing η, in contrast to what happens for $\epsilon \gtrsim 1$. For no-slip boundary conditions, similar diagrams are obtained. The numerical results show that the transition line between multicellular modes with n and $n+1$ maxima of $|\Psi(x)|$ follow, for small P, a scaling law of the form

$$\eta_n^{n+1} \propto 1/P. \tag{3.1}$$

The purpose of the asymptotic theory to be developed in the following sections is to explain this scaling law, to identify the multicellular modes as quasi-inertial modes, and to elucidate the physical mechanisms leading to the diagram of figure 4. For this we will follow the pioneering works of Yano (1992) and Zhang (1993, 1994).

4. Inertial modes in the stress-free case

Since, for small Prandtl numbers, dissipation and buoyancy are small in comparison to the inertial terms in (2.8a), a perturbation approach,

$$\Psi = \Psi_0 + \Psi_1 + \cdots, \quad \omega = \omega_0 + \omega_1 + \cdots, \tag{4.1}$$

can be used where the inertial mode streamfunction $\Psi_0(x)$ satisfies (2.8a) in the absence of dissipation and buoyancy,

$$\partial_x^2 \Psi_0 = -(\alpha\eta\epsilon/\omega_0)(x - x_0)\Psi_0 \quad \text{with } x_0 = \alpha\omega_0/(\eta\epsilon) - 1/\epsilon. \tag{4.2}$$

Through the transformation

$$x - x_0 = -(\alpha\eta\epsilon/\omega_0)^{-1/3}\xi, \tag{4.3}$$

the real Airy equation

$$\partial_\xi^2 \Psi_0 = \xi \Psi_0 \tag{4.4}$$

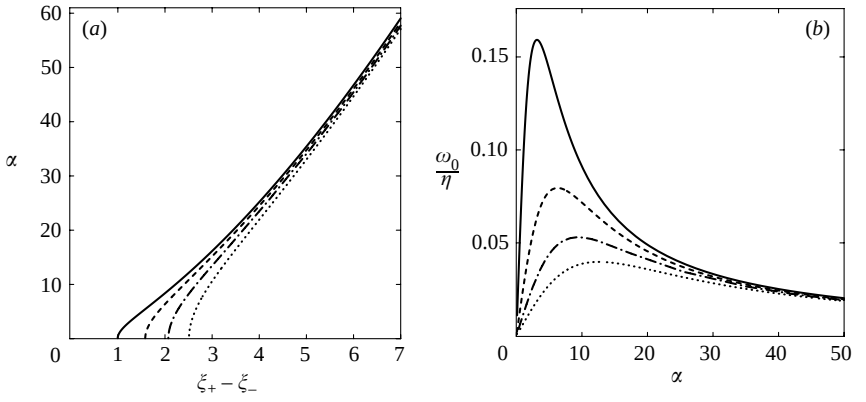

FIGURE 5. Characteristics of the inertial modes for $\epsilon = 0.1$, and, from top to bottom, $n = 1, 2, 3, 4$. (*a*) Wavenumber as a function of $\xi_+ - \xi_-$ according to (4.7*a*). (*b*) Dispersion relation (4.7*b*).

is obtained. Because of the boundary conditions (2.9*a*), $\Psi_0(\xi)$ must vanish at

$$\xi_\pm = (\alpha\eta\epsilon/\omega_0)^{1/3}(x_0 \pm 1/2). \tag{4.5}$$

$\Psi_0(\xi)$ thus assumes the form of a combination of the two Airy functions

$$\Psi_0(\xi) = \mathrm{Ai}(\xi) - \mathrm{Ai}(\xi_+)\mathrm{Bi}(\xi)/\mathrm{Bi}(\xi_+), \tag{4.6}$$

with condition $\Psi_0(\xi_-) = 0$ determining discrete values ξ_-^n of ξ_-. Here, $n - 1 \in \mathbb{N}$ denotes the number of zeros of $\Psi_0(\xi)$ within the interval $\xi_-^n < \xi < \xi_+$. Infinite manifolds of solutions $\Psi_0(x; \xi_+, n)$ are thus obtained. For each class the wavenumber and the frequency of the inertial modes can be deduced from (4.5),

$$\alpha^2 = (\xi_+ - \xi_-)^3/\epsilon + (\xi_+ + \xi_-)(\xi_+ - \xi_-)^2/2, \tag{4.7a}$$

$$\omega_0 = \alpha\eta\epsilon/(\xi_+ - \xi_-)^3. \tag{4.7b}$$

An example of a solution for $n = 4$ is shown in figure 3(*d*), where the streamfunction has been normalized. Since the streamfunction $\Psi_0(x)$ is real, the separatrices of the corresponding flow given by

$$\psi_0(x, y, t) = 2\mathrm{Re}\{\Psi_0(x)\exp[\mathrm{i}(\alpha y - \omega_0 t)]\} = 2\Psi_0(x)\cos(\alpha y - \omega_0 t)$$

are straight lines aligned with the coordinate axes as displayed in figure 3(*c*). In equation (4.7*a*) the first term on the right-hand side is always positive, whereas the second term may assume either sign. The form of the first term shows clearly that larger curvature effects, i.e. larger ϵ, tend to diminish the wavenumber, i.e. to increase the wavelength of the inertial modes. It is also worth noting that the streamfunction and wavenumber of a particular inertial mode do not depend on the Coriolis parameter η while ω_0 is proportional to η. The fact that ω_0 is positive for positive ϵ indicates a prograde propagation. Illustrative results for α and ω_0/η are displayed in figures 5 and 6 for representative values of ϵ, $\xi_+ - \xi_-$ and n. They clearly show that larger n, i.e. larger $\xi_+ - \xi_-$, leads to smaller frequencies.

To each inertial mode there corresponds a temperature modulation $\Theta_0(x)\exp[\mathrm{i}(\alpha y - \omega_0 t)]$ determined by the heat equation (2.8*b*),

$$\left(\partial_x^2 - \alpha^2 + \mathrm{i}\omega_0 P\right)\Theta_0(x) = \mathrm{i}\alpha\Psi_0(x). \tag{4.8}$$

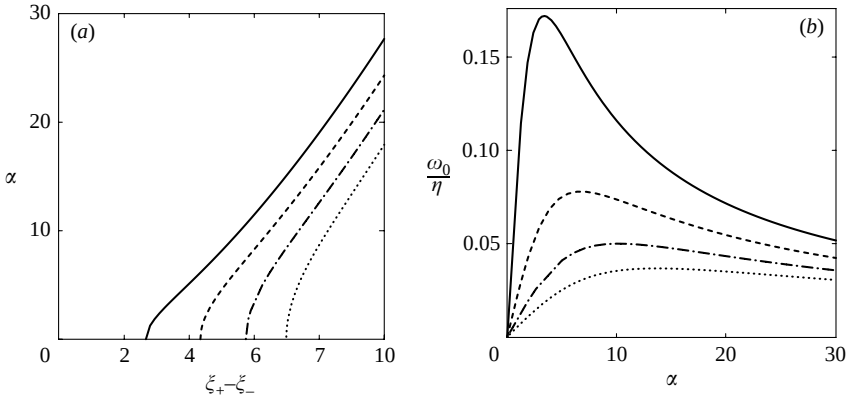

FIGURE 6. As figure 5, but for a larger curvature parameter $\epsilon = 2$.

Together with the isothermal boundary conditions, this equation can be solved easily with a Galerkin method. In contrast to Ψ_0, Θ_0 has a non-vanishing imaginary part and does depend on η; in fact, because of (4.7b), Θ_0 depends only on the product ηP.

5. Inertial convection in the stress-free case

The solutions obtained in the preceding section form the basis for the description of convection at low Prandtl number with the perturbation approach (4.1). The equation for the perturbation $\Psi_1(x)$ of $\Psi_0(x)$ reads

$$\left[\mathrm{i}\omega_0\left(\partial_x^2 - \alpha^2\right) + \mathrm{i}\alpha\eta(1+\epsilon x)\right]\Psi_1 = -\left(\partial_x^2 - \alpha^2\right)^2\Psi_0 + \mathrm{i}\alpha R\Theta_0 - \mathrm{i}\omega_1\left(\partial_x^2 - \alpha^2\right)\Psi_0. \quad (5.1)$$

Multiplication with $\Psi_0(x)$ and integration over the interval $-1/2 \leqslant x \leqslant 1/2$, as indicated by the angle brackets, yields the solvability condition

$$\mathrm{i}\alpha R\left\langle\Psi_0\Theta_0\right\rangle - \mathrm{i}\omega_1\left\langle\Psi_0\left(\partial_x^2 - \alpha^2\right)\Psi_0\right\rangle = \left\langle\Psi_0\left(\partial_x^2 - \alpha^2\right)^2\Psi_0\right\rangle. \quad (5.2)$$

Introducing the dissipation, inertia and buoyancy integrals

$$D = \left\langle\Psi_0\left(\partial_x^2 - \alpha^2\right)^2\Psi_0\right\rangle = (\alpha\eta/\omega_0)^2\langle[(1+\epsilon x)\Psi_0]^2\rangle, \quad (5.3a)$$

$$I = -\left\langle\Psi_0\left(\partial_x^2 - \alpha^2\right)\Psi_0\right\rangle = (\alpha\eta/\omega_0)\left\langle(1+\epsilon x)\Psi_0^2\right\rangle, \quad (5.3b)$$

$$B_r = \langle\Psi_0\mathrm{Re}(\Theta_0)\rangle, \quad (5.3c)$$

$$B_i = -\langle\Psi_0\mathrm{Im}(\Theta_0)\rangle, \quad (5.3d)$$

we thus obtain

$$R = D/(\alpha B_i), \quad \omega_1 = -\alpha R B_r/I, \quad (5.4)$$

which shows that the neutral Rayleigh number R is governed by a balance between dissipation and buoyancy, and the frequency shift ω_1 by a balance between buoyancy and inertia. Since the Prandtl number enters the analysis only through the function Θ_0, i.e. through the product ηP, R and ω_1 depend only on the combination ηP. The numerical results of the Galerkin code summarized in figure 4, which show that, in the limit $P \to 0$, the neutral Rayleigh numbers of the various competing equatorially attached modes depend only on ηP, suggest that they approach asymptotically the inertial modes that we have calculated. This is confirmed by quantitative comparisons, like those presented in figures 7 and 8. In these figures the Rayleigh numbers

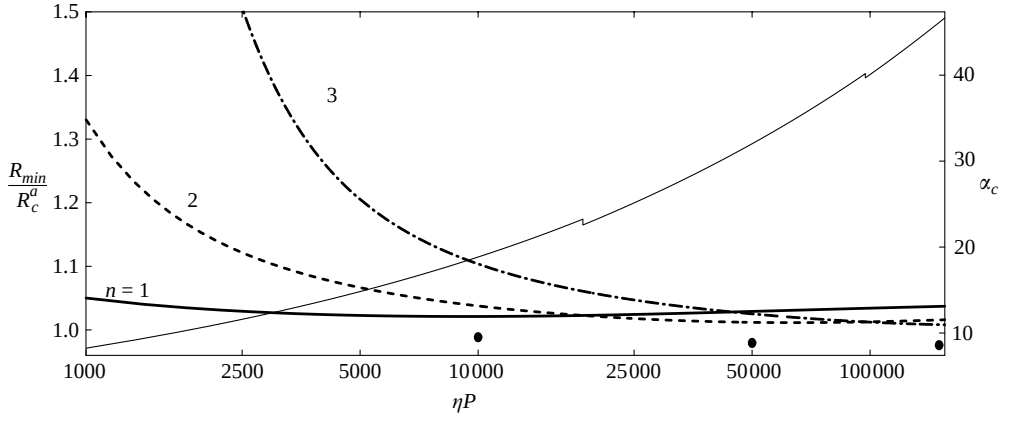

FIGURE 7. Results of the perturbation theory for the inertial convection modes in the stress-free case and for $\epsilon = 0.1$: reduced values of the neutral Rayleigh numbers after minimization *vs.* α (thick lines, left-hand axis); corresponding critical wavenumbers (thin line, right-hand axis). Note the jumps of α_c at the points where lines with n and $n+1$ intersect. The circles show for comparison some reduced numerical values of R_c obtained with the linear Galerkin code for $P = 0.025$.

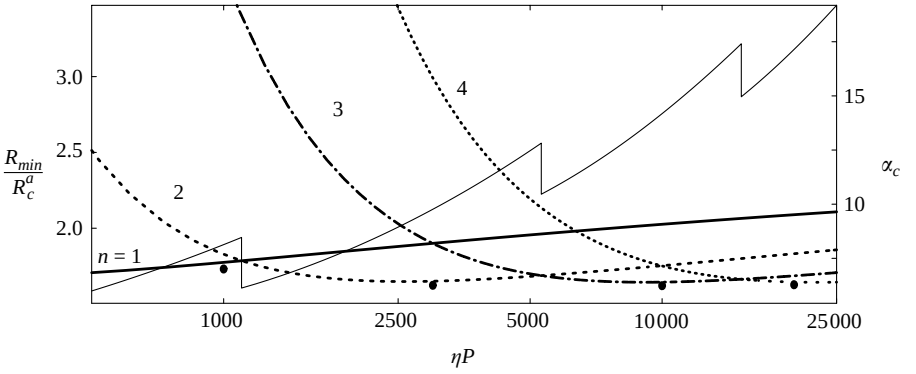

FIGURE 8. As figure 7, but for $\epsilon = 2$. Corresponding critical frequencies are displayed in figure 9.

minimized as a function of α, divided by

$$R_c^a = 3(\eta P/\sqrt{2})^{4/3} \tag{5.5}$$

which is the asymptotic expression obtained in the case $\epsilon = 0$ in the limit of large η and small P (Busse & Or 1986), have been plotted for different values of n. Figure 8 has been complemented with figure 9, showing the corresponding critical frequencies $\omega_c = \omega_0(\alpha_c) + \omega_1(\alpha_c)$ in the perturbation theory; note that ω_1 always represents a small negative correction to ω_0. At the test points shown, for $P = 0.025$, the relative errors on R_c are less than 3.3%, the relative errors on α_c less than 2.1%, and the relative errors on ω_c less than 0.9%. Naturally, the agreement between the perturbation theory and the numerical results becomes better for smaller Prandtl numbers.

For large η, the decrease of the Rayleigh number $R = D/(\alpha B_i)$ with increasing n, visible in figures 7 and 8, stems from the fact that, while D increases with increasing n, it does so less sharply than B_i. Since D is the power consumed by viscous dissipation

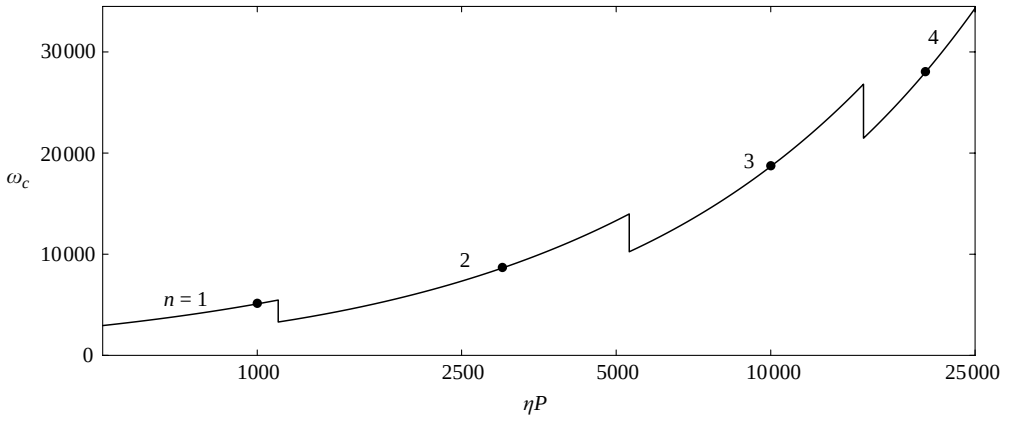

FIGURE 9. Critical frequencies $\omega_0(\alpha_c)+\omega_1(\alpha_c)$ corresponding to the sequence of critical modes of figure 8 for $P=0.025$. The circles show some numerical values of ω_c obtained with the linear Galerkin code.

and $R\alpha B_i$ the power developed by the buoyancy forces, this means that the increased dissipation in multicellular modes is overcome by a much more efficient release of buoyancy. This latter effect arises because, according to (4.8), the reduced buoyancy force

$$-\Theta_0 = \left(\alpha^2 - \partial_x^2 - \mathrm{i}\omega_0 P\right)^{-1} \mathrm{i}\alpha\Psi_0$$

is larger and more 'in phase' with the radial component of the flow $\mathrm{i}\alpha\Psi_0$ for increasing n. This, in turn, is due essentially to the strong decrease of the angular frequency ω_0 with increasing n, visible in figures 5(b) and 6(b). These effects also exist in the absence of curvature, $\epsilon=0$, and are responsible for the property that the critical values of the Rayleigh number are asymptotically independent of n (Busse 1986). In the case of finite curvature, $\epsilon\neq 0$, the decrease of ω_0 with increasing n is sharper (compare figures 5b and 6b), and thus the multicellular modes, which, moreover, can adjust better to the inhomogeneous conditions of the annular gap, are typically preferred.

While these results explain the properties of quasi-inertial convection at small Prandtl numbers as displayed in figure 4, together with the scaling law (3.1), the onset of spiralling modes cannot be captured by the perturbation theory, which confirms that these latter modes are not governed by inertia.

Finally, it is worth mentioning that, just as (5.5) describes the order of magnitude of R_c, the asymptotic values

$$\alpha_c^a = 2^{-1/6} P^{1/3} \eta^{1/3}, \quad \omega_c^a = 2^{1/6} P^{-1/3} \eta^{2/3} \tag{5.6}$$

derived in Busse & Or (1986) for the case $\epsilon=0$ give the correct order of magnitude for the values of α_c and ω_c obtained for small P and large η in the interval $0\leqslant\epsilon\leqslant 2$.

6. The effect of no-slip boundary conditions

The results obtained in the preceding sections are valid when the velocity field satisfies stress-free conditions at the cylindrical walls $x=\pm 1/2$. Although the inertial modes do not need to satisfy the condition $\partial_x^2\Psi=0$ at $x=\pm 1/2$, they do so by virtue of Airy's equation. At rigid walls the condition $\partial_x\Psi=0$ at $x=\pm 1/2$ must be satisfied in addition to the condition $\Psi=0$ at $x=\pm 1/2$. In order to accommodate the no-slip condition the inertial mode streamfunction $\Psi_0(x)$ must be modified by boundary-layer

contributions $\widetilde{\Psi}(x)$ which are governed by the equation

$$\mathrm{i}\omega_0\widetilde{\Psi}'(x) = -\widetilde{\Psi}'''(x). \tag{6.1}$$

where the prime indicates the derivative. In writing this equation we are anticipating that $\widetilde{\Psi}(x)$ is finite only in small boundary layers of thickness $\omega_0^{-1/2}$ adjacent to the walls at $x = \pm 1/2$. Since, for small values of P, the inequality $\alpha_c^2 \ll \omega_0$ is always satisfied, the tangential component of the velocity field is much larger than the normal component and the Coriolis force is thus directed mainly normal to the wall and balanced by the pressure gradient. Equation (6.1) thus represents the dominating terms of the azimuthal component of the Navier–Stokes equation in the boundary layers. Solutions of (6.1) can be written in the form

$$\widetilde{\Psi}_{\pm}(x) = p_{\pm}\exp[\pm(1-\mathrm{i})\sqrt{\omega_0/2}(x \mp 1/2)] \tag{6.2}$$

near $x = \pm 1/2$. The condition $\Psi_0'(x) + \widetilde{\Psi}_{\pm}'(x) = 0$ at $x = \pm 1/2$ yields

$$p_{\pm} = \mp\Psi_0'(\pm 1/2)/[(1-\mathrm{i})\sqrt{\omega_0/2}]. \tag{6.3}$$

Of course, $\Psi_0(x) + \widetilde{\Psi}_{\pm}(x)$ no longer vanishes at $x = \pm 1/2$ and a further contribution to the streamfunction is required in order to rectify this situation. Since the amplitudes p_+ and p_- are only of the order $\omega_0^{-1/2}$, this correction will lead to a negligible change of the Rayleigh number. The evaluation of the additional term $\langle \Psi_0(\partial_x^2 - \alpha^2)^2\widetilde{\Psi}\rangle$ in the solvability condition (5.2) yields

$$\left\langle \Psi_0\left(\partial_x^2 - \alpha^2\right)^2\widetilde{\Psi}\right\rangle = -\left[(\partial_x\Psi_0)\left(\partial_x^2\widetilde{\Psi}\right)\right]_{-1/2}^{1/2} + h.o.t. = (1-\mathrm{i})\widetilde{D} + h.o.t. \tag{6.4}$$

with

$$\widetilde{D} = \sqrt{\omega_0/2}\{[\Psi_0'(1/2)]^2 + [\Psi_0'(-1/2)]^2\}. \tag{6.5}$$

Instead of (5.4) we now obtain from the solvability condition (5.2) and to leading order

$$R = (D + \widetilde{D})/(\alpha B_i), \quad \omega_1 = -\alpha R B_r/I - \widetilde{D}/I, \tag{6.6}$$

which clearly show the effects of the increased dissipation in the boundary layers on the neutral Rayleigh number and frequency shift of the no-slip convection modes. Minimizing the Rayleigh number *vs.* n and α leads to a good estimate of the critical properties of no-slip convection as compared with the linear Galerkin code. For instance, for the same test points as those shown in figures 7 and 8, the relative errors on R_c are less than 3.8%, the relative errors on α_c less than 2.3%, and the relative errors on ω_c less than 1.1%.

7. Geometrical study of the mean zonal flow

The most interesting nonlinear effect proportional to the square of the amplitude of the critical mode is surely the generation of the azimuthal mean flow $u(x)$ by the nonlinear advection term $S(x)$, as expressed by the azimuthal average of the azimuthal Navier–Stokes equation (see e.g. Plaut & Busse 2002)

$$\partial_x^2 u = S = 2\alpha_c \mathrm{Im}[\partial_x(\Psi\partial_x\Psi^*)]. \tag{7.1a}$$

Plaut & Busse (2002) showed that the source term $S(x)$ has a geometrical meaning in terms of the separatrices $y(x)$, the streamlines $\psi(x, y, t) = 0$,

$$\partial_x^2 u = S = 2\alpha_c^2\partial_x(|\Psi|^2 y') = 2\alpha_c^2[|\Psi|^2 y'' + 2\mathrm{Re}(\Psi^*\Psi')y'], \tag{7.1b}$$

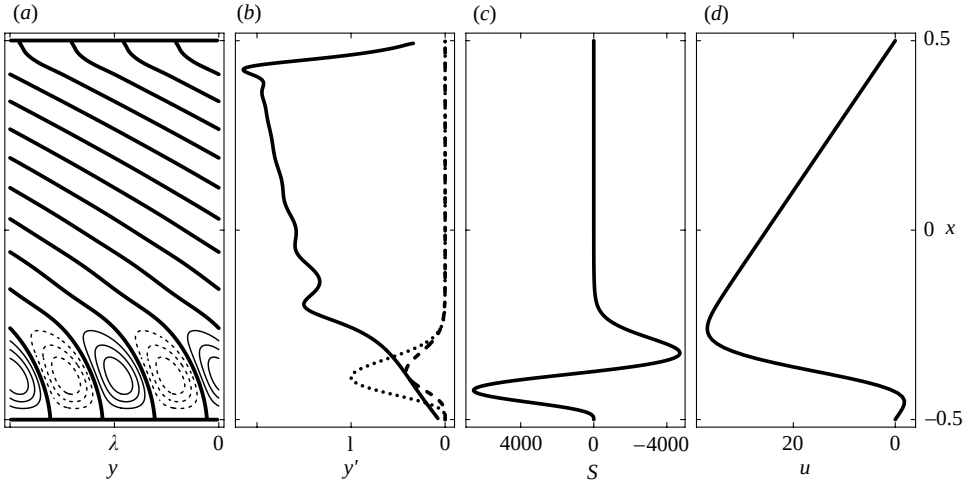

FIGURE 10. Spiralling critical mode computed with the Galerkin code for no-slip boundary conditions, $\epsilon = 2$, $P = 7$, $\eta = 206\,000$, with its associated mean zonal flow. (*a*) Streamlines; the thick lines show the separatrices $y(x)$. The wavelength $\lambda = 0.278$. (*b*) —, slope $y'(x)$ of the separatrices; $\cdots$, square of the modulus of the streamfunction $|\Psi(x)|^2$; ---, product $|\Psi(x)|^2 y'(x)$. (*c*) Source term $S(x)$ from (7.1). (*d*) Corresponding mean flow obtained by a numerical solution of (7.1) with the boundary conditions (7.2). Note that, when Ekman friction effects are taken into account (see § 8), the mean-flow is no longer given by (*d*), but instead by $-\tau_E S$, i.e. its form is given by (*c*).

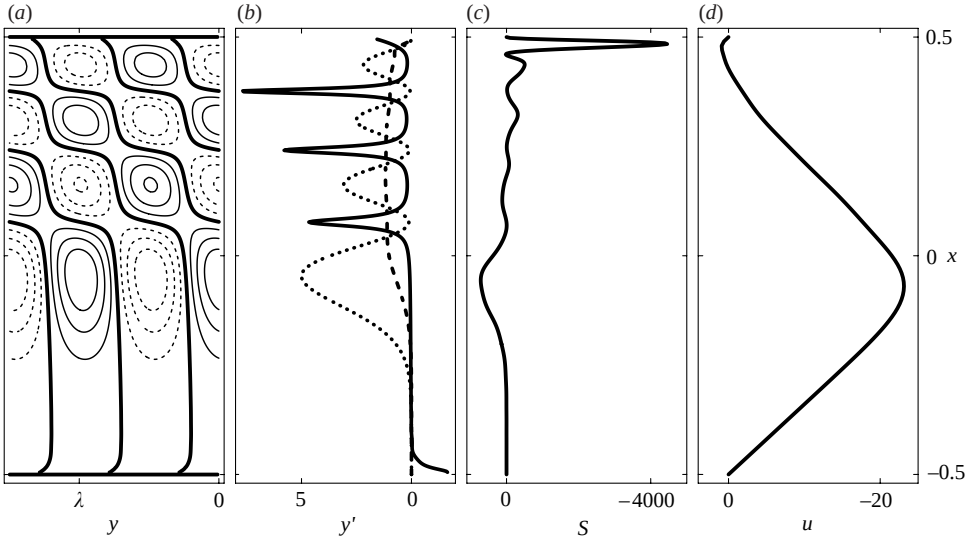

FIGURE 11. As figure 10, but for a multicellular equatorially attached critical mode computed for no-slip boundary conditions, $\epsilon = 2$, $P = 0.025$, $\eta = 800\,000$. (*a*) Streamlines. The wavelength $\lambda = 0.322$. (*b*) —, $y'(x)$; $\cdots$, $5|\Psi(x)|^2$; ---, $10|\Psi(x)|^2 y'(x)$. (*c*) Source term $S(x)$. (*d*) Corresponding mean flow.

where, in fact, $-2\alpha_c^2|\Psi|^2 y'$ is the relevant Reynolds stress, the azimuthal average of $-v_x v_y$. However, the consequences of the general relation (7.1*b*) in the presence of curvature effects were not studied. This gap is filled by figures 10 and 11 for a spiralling

and an equatorially attached mode. In both cases we focus on no-slip boundary conditions,

$$u = 0 \quad \text{at } x = \pm\tfrac{1}{2}, \tag{7.2}$$

and a Galerkin code has been used to compute the critical modes and to integrate (7.1), (7.2). For the spiralling mode (figure 10), the source term is non-vanishing only near the inner cylinder because of its proportionality to $\Psi(x)$, and in fact the form of the function $S(x)$ is mainly controlled by the factor $|\Psi(x)|^2$, since, in the inner region, $y'(x)$ is approximately constant. Indeed, using the approximation $y'(x) \simeq y'_0$ in the inner region, we obtain $S(x) \simeq 2\alpha_c^2 y'_0 \partial_x(|\Psi|^2)$ from (7.1*b*), which does explain the shape of the source term shown in figure 10(*c*). For the equatorially attached mode, on the contrary, the source term is stronger in the boundary layer of the outer cylinder (figure 11*c*). The function $S(x)$ also presents several oscillations because of the complex structure of the functions $|\Psi(x)|^2$ and $y'(x)$ displayed in figure 11(*b*). However, the double integration over the x-coordinate yields in both cases a mean flow $u(x)$ of a rather smooth and simple form, shown in figures 10(*d*) and 11(*d*).

8. The influence of Ekman friction

The above results must be revisited if we take into account the effects of the Ekman friction at the conical caps, which we have neglected up to now. This is, in general, justified for the calculation of neutral modes, for which the dissipation due to viscous stress associated with azimuthal velocity gradients, i.e. the terms proportional to α^2 and α^4 in the right-hand side of (2.8*a*), of order $E^{-4/3}$ typically, dominate the Ekman friction effect of order $E^{-1/2}$. On the other hand, as pointed out by Soward (1977) and Aubert *et al.* (2003), Ekman friction effects on the mean flow are typically non-negligible, since the mean flow does not create viscous stress associated with azimuthal velocity gradients. In order to calculate the quadratic mean flow, we should therefore not solve (7.1) but instead (Greenspan 1968)

$$\partial_x^2 u - u/\tau_E = S, \tag{8.1}$$

where the 'Ekman friction time'

$$\tau_E = (h/d)E^{1/2}. \tag{8.2}$$

For the geometrical parameters of the outer core of the Earth, $h \simeq d$, $\eta_0 \simeq 1$, $E \simeq 2/\eta$, the Ekman friction term roughly dominates the viscous term $\partial_x^2 u$ in (8.1). Consequently, we are led to the rough approximation

$$u \simeq -\tau_E S = -2\tau_E \alpha_c^2 \partial_x(|\Psi|^2 y'), \tag{8.3}$$

which dramatically changes the simple pictures of figures 10(*d*) and 11(*d*). Application of (8.3) to the spiralling mode of figure 10 yields a zonal flow very similar to that obtained with the model of Aubert *et al.* (2003) in their figure 7(*a*). This indicates that the geometrical analysis developed here is also relevant for their model, despite the fact that they have a large gap. In the case of the multicellular mode of figure 11, a 'multijet' zonal flow is obtained, with a strong jet near the outer cylinder.

9. Discussion

One would like to study, in the model including Ekman friction, higher nonlinear effects such as the saturation of the critical wave, its stability versus long-wavelength

perturbations, and other secondary instabilities. Indeed, especially at small P, mean-flow effects are known to play an important role at this stage (see e.g. Or & Busse 1987; Abdulrahman *et al.* 2000; Plaut & Busse 2002). However, a numerical solution of the full equation (8.1) and a heavy computational effort will be required since, even for the case of an equatorially attached critical mode, the problem depends on the parameters η and P separately now instead of on their combination ηP only.

Another prospect opened by the present work concerns the systematic study of multicell modes in spherical shell convection and at small Prandtl numbers, which has not yet been done. A perturbation theory based on the inertial wave representation developed by Zhang *et al.* (2001) for a rotating fluid sphere will be an interesting challenge for future research.

We acknowledge support from the Conseil Régional de Lorraine with a grant Accueil de Chercheurs Etrangers.

Appendix. The limit of vanishing curvature

Let us show that, in the stress-free case, the limit $\epsilon \to 0$ is regular, i.e. we obtain from the general expressions (4.7) and (5.4) the analytical expressions for $\epsilon = 0$ derived in Busse & Or (1986). In the limit $\epsilon \to 0$, the relevant inertial modes fulfil $\xi_0 = |\xi_+ + \xi_-|/2 \gg 1$ and $\mathrm{Ai}(\xi_+) = \mathrm{Ai}(\xi_-) = 0$ to good approximation. Hence, according to the asymptotic representation of the Airy function (Abramowitz & Stegun 1972), $|\xi_-|^{3/2} - |\xi_+|^{3/2} = 3n\pi/2$ holds. We thus find $\xi_+ - \xi_- = n\pi/\xi_0^{1/2}$. As a consequence, (4.7) can be written in the form

$$\alpha^2 = \alpha\eta/\omega_0 - n^2\pi^2, \quad \omega_0 = \alpha\eta\epsilon\xi_0^{3/2}/(n\pi)^3, \tag{A 1}$$

from which the dispersion relation $\omega_0 = \alpha\eta/(\alpha^2 + n^2\pi^2)$ for thermal Rossby waves in the limit $P = 0$ (Busse & Or 1986) follows. We may also conclude from (A 1) that ξ_0 tends to infinity as ϵ approaches zero in such a way that $\epsilon\xi_0^{3/2}$ stays constant. Since, in the limit $\epsilon \to 0$, we have $\langle[(1+\epsilon x)\Psi_0]^2\rangle = \langle\Psi_0^2\rangle$, and moreover, according to (4.8),

$$\begin{aligned}\langle\Theta_0\Psi_0\rangle - \alpha/(\omega_0 P)\langle\Psi_0^2\rangle &= \mathrm{i}/(\omega_0 P)\langle\Psi_0(\partial_x^2 - \alpha^2)\Theta_0\rangle \\ &= \mathrm{i}/(\omega_0 P)\langle\Theta_0(\partial_x^2 - \alpha^2)\Psi_0\rangle = -\mathrm{i}\alpha\eta/(\omega_0^2 P^2)\langle\Theta_0\Psi_0\rangle,\end{aligned}$$

the expressions (5.4) for R and ω_1 can easily be evaluated to lowest order in ϵ,

$$R = (\alpha\eta/\omega_0)^2\left[\omega_0^3 P^2/(\alpha^3\eta) + \eta/(\omega_0\alpha)\right] = \eta^2 P^2/(\alpha^2 + n^2\pi^2) + (\alpha^2 + n^2\pi^2)^3/\alpha^2,$$
$$\omega_1 = -\omega_0 P.$$

These represent the correct expressions for the Rayleigh number and for the first-order correction of the frequency ω at small Prandtl numbers P in the case $\epsilon = 0$.

REFERENCES

Abdulrahman, A., Jones, C. A., Proctor, M. R. E. & Julien, K. 2000 Large wavenumber convection in the rotating annulus. *Geophys. Astrophys. Fluid Dyn.* **93**, 227.

Abramowitz, M. & Stegun, I. A. 1972 *Handbook of Mathematical Functions*. Dover.

Ardes, M., Busse, F. H. & Wicht, J. 1997 Thermal convection in rotating spherical shells. *Phys. Earth Planet. Inter.* **99**, 55.

Aubert, J., Gillet, N. & Cardin, P. 2003 Quasigeostrophic models of convection in rotating spherical shells. *Geochem. Geophys. Geosyst.* **4**, 1052.

Busse, F. H. 1970 Thermal instabilities in rapidly rotating systems. *J. Fluid Mech.* **44**, 441.

Busse, F. H. 1986 Asymptotic theory of convection in a rotating, cylindrical annulus. *J. Fluid Mech.* **173**, 545.

Busse, F. H. & Or, A. C. 1986 Convection in a rotating cylindrical annulus: thermal Rossby waves. *J. Fluid Mech.* **166**, 173.

Busse, F. H. & Simitev, R. 2004 Inertial convection in rotating fluid spheres. *J. Fluid Mech.* **498**, 23.

Dormy, E., Soward, A. M., Jones, C. A., Jault, D. & Cardin, P. 2004 The onset of thermal convection in rotating spherical shells. *J. Fluid Mech.* **501**, 43.

Greenspan, H. P. 1968 *The Theory of Rotating Fluids*. Cambridge University Press.

Jones, C. A., Soward, A. M. & Mussa, A. I. 2000 The onset of thermal convection in a rapidly rotating sphere. *J. Fluid Mech.* **405**, 157.

Morin, V. & Dormy, E. 2004 Time dependent β-convection in rapidly rotating spherical shells. *Phys. Fluids* **16**, 1603.

Or, A. C. & Busse, F. H. 1987 Convection in a rotating cylindrical annulus. Part 2. Transitions to asymmetric and vacillating flow. *J. Fluid Mech.* **174**, 313.

Pino, D., Mercader, I. & Net, M. 2000 Thermal and inertial modes of convection in a rapidly rotating annulus. *Phys. Rev.* E **61**, 1507.

Pino, D., Net, M., Sánchez, J. & Mercader, I. 2001 Thermal Rossby waves in a rotating annulus. Their stability. *Phys. Rev.* E **63**, 056312.

Plaut, E. & Busse, F. H. 2002 Low-Prandtl-number convection in a rotating cylindrical annulus. *J. Fluid Mech.* **464**, 345.

Simitev, R. & Busse, F. H. 2004 Patterns of convection in rotating spherical shells. *New J. Phys.* **5**, 97.

Soward, A. M. 1977 On the finite amplitude thermal instability of a rapidly rotating fluid sphere. *Geophys. Astrophys. Fluid Dyn.* **9**, 19.

Westerburg, M. & Busse, F. H. 2003 Centrifugally driven convection in the rotating cylindrical annulus with modulated boundaries. *Nonlinear Proc. Geophys.* **10**, 275.

Yano, J. I. 1992 Asymptotic theory of thermal convection in rapidly rotating systems. *J. Fluid Mech.* **243**, 103.

Zhang, K. 1992 Spiralling columnar convection in rapidly rotating spherical fluid shells. *J. Fluid Mech.* **236**, 535.

Zhang, K. 1993 On equatorially trapped boundary inertial waves. *J. Fluid Mech.* **248**, 203.

Zhang, K. 1994 On coupling between the Poincaré equation and the heat equation. *J. Fluid Mech.* **268**, 211.

Zhang, K. & Busse, F. H. 1987 On the onset of convection in rotating spherical shells. *Geophys. Astrophys. Fluid Dyn.* **39**, 119.

Zhang, K., Earnshaw, P., Liao, X. & Busse, F. H. 2001 On inertial waves in a rotating fluid sphere. *J. Fluid Mech.* **437**, 103.